Nanoscale

PAPER

View Article Online
View Journal | View Issue

Cite this: *Nanoscale*, 2017, **9**, 13670

Nanostructured interfacial self-assembled peptide–polymer membranes for enhanced mineralization and cell adhesion†

Sofia Ribeiro, [a,b] Elham Radvar, [c,d] Yejiao Shi, [c,d] João Borges, [e] Rogério P. Pirraco, [a,b] Isabel B. Leonor, [a,b] João F. Mano, [e] Rui L. Reis, [a,b] Álvaro Mata [c,d] and Helena S. Azevedo *[a,b,c,d]

Soft interfacial materials, such as self-assembled polymer membranes, are gaining increasing interest as biomaterials since they can provide selective barriers and/or controlled affinity interactions important to regulate cellular processes. Herein, we report the design and fabrication of multiscale structured membranes integrating selective molecular functionalities for potential applications in bone regeneration. The membranes were obtained by interfacial self-assembly of miscible aqueous solutions of hyaluronan and multi-domain peptides (MDPs) incorporating distinct biochemical motifs, including mineralizing (EE), integrin-binding (RGDS) and osteogenic (YGFGG) peptide sequences. Circular dichroism and Fourier transform infrared spectroscopy analyses of the MDPs revealed a predominant β-sheet conformation, while transmission electron microscopy (TEM) showed the formation of fibre-like nanostructures with different lengths. Scanning electron microscopy (SEM) of the membranes showed an anisotropic structure and surfaces with different nanotopographies, reflecting the morphological differences observed under TEM. All the membranes were able to promote the deposition of a calcium-phosphate mineral on their surface when incubated in a mineralizing solution. The ability of the MDPs, coated on coverslips or presented within the membranes, to support cell adhesion was investigated using primary adult periosteum-derived cells (PDCs) under serum-free conditions. Cells on the membranes lacking RGDS remained round, while in the presence of RGDS they appear to be more elongated and anchored to the membrane. These observations were confirmed by SEM analysis that showed cells attached to the membrane and exhibiting an extended morphology with close interactions with the membrane surface. We anticipate that these molecularly designed interfacial membranes can both provide relevant biochemical signals and structural biomimetic components for stem cell growth and differentiation and ultimately promote bone regeneration.

Received 13th May 2017,
Accepted 15th August 2017

DOI: 10.1039/c7nr03410e

rsc.li/nanoscale

1 Introduction

Interfaces (solid/liquid, gas/liquid, gas/solid, liquid/liquid) have been widely used as fabrication platforms for the *in situ* generation of advanced materials with specific properties and functions. For instance, the interfacial tension formed between two immiscible liquids has been exploited to carry out reactions and polymerizations[1] at the boundary phase or to promote the assembly of polymers and proteins into diverse multifunctional structures. Some examples of these interfacial reactions and assemblies, and their broad utility, are the polycondensation of nylon, microcapsules with the ability to trap and control the release of cargos on demand[2] or biomimetic protocells capable of storage, selective permeability and replication.[3] The properties of interfaces can be made highly reproducible and tuned to manipulate local interactions and drive the assembly of materials with controlled porosities and defined geometries (*e.g.* films formed at planar rigid substrates or spherical capsules formed at the droplet interface).[4] Assembly of films, capsules, and fibres at the interface

[a]*3B's Research Group – Biomaterials, Biodegradables and Biomimetics, Headquarters of the European Institute of Excellence on Tissue Engineering and Regenerative Medicine, University of Minho, AvePark, 4806-909 Taipas, Guimarães, Portugal. E-mail: h.azevedo@qmul.ac.uk*
[b]*ICVS/3B's – PT Government Associate Laboratory, Braga/Guimarães, Portugal*
[c]*School of Engineering and Materials Science, Queen Mary University of London, London E1 4NS, UK*
[d]*Institute of Bioengineering, Queen Mary University of London, London E1 4NS, UK*
[e]*Department of Chemistry, CICECO – Aveiro Institute of Materials, University of Aveiro, 3810-193 Aveiro, Portugal*
†Electronic supplementary information (ESI) available. See DOI: 10.1039/c7nr03410e

between miscible aqueous liquids has also been reported using polyelectrolyte complexes (PECs) in a single step[5,6] or through layer-by-layer (LbL) deposition using a solid template.[7–9] A major advantage of PEC-based approaches consists of the mild conditions (aqueous solution, neutral pH, and room temperature) used during the assembly process[7] allowing the direct incorporation of delicate bioentities, such as enzymes,[10] growth factors,[11] and cells.[12] However, materials formed from PECs do not present internal order[5,13,14] and the resulting assemblies typically require post crosslinking (ionic, chemical or photo-induced) to prevent dissolution or dissociation under ionic strength close to the physiological conditions. In addition, LbL assembly is a time intensive multistep process (layer build-up and intermediate washings). In 2008, Stupp and co-workers reported the formation of stable and highly organized membranes at the interface of two miscible liquids, one containing a large polysaccharide and the other containing small peptide amphiphiles (PAs).[15] Since then, our groups and others have been exploring interfacial self-assembly of PAs with various macromolecules, including hyaluronan (HA),[16–18] alginate,[19–21] and elastin-like proteins,[22] to develop a range of macroscopic biomaterials, including membranes, sacs/capsules and tubes, with strong application potential in tissue engineering. We have previously shown the formation of thin membranes by interfacial self-assembly,[23] combining positively charged multi-domain peptides (MDPs), proposed by Hartgerink *et al.*,[24] with the negatively charged biopolymer HA. The initial MDP design was based on the model sequence $K_2(QL)_6K_2$ (Fig. 1) consisting of alternating hydrophobic (leucine, L) and hydrophilic (glutamine, Q) residues in the centre and positively charged residues (lysine, K) in the flanking sides. This design creates two distinct faces, a hydrophobic face with leucine side chains on one side and a hydrophilic face formed by glutamine side chains on the other side, while the charged groups provide peptide solubility and hinder self-assembly. In aqueous solution, the two hydrophobic faces pack together generating a hydrophobic sandwich that supports and stabilises the extending structure. When the charges are screened by counterions (oppositely charged multivalent ions, such as PO_4^{3-}), the MDPs form nanofibre hydrogels through self-assembly. Building on this first design, several sequence variations have been explored to modulate the mechanical and biological functionalities of the resulting gels for different biological applications.[25–28] These studies demonstrate that MDPs can tolerate a wide variety of modifications, while retaining their basic nanofiber structure and desired bioactivity. The fabrication of synthetic membranes *via* self-assembly is very appealing due to its low-cost and ability to create inbuilt order by combining properties of different building blocks.[29] Self-assembling peptide–polymer hybrid membranes present advantageous physical and chemical features. They are formed spontaneously in a single step and can be assembled *in situ* in the physiological environment. Because peptides can be customized to display specific bio-

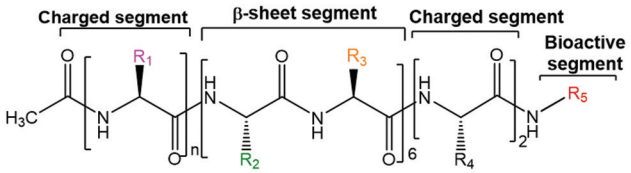

MDP	R_1	R_2	R_3	R_4	R_5	Net charge pH 7	Zeta potential [mV] pH 7
$K_2(QL)_6K_2$	n = 2				None	+4	65.70±2.8
$K_2(SV)_6K_2$	n = 2				None	+4	48.10±1.3
$K_3(QL)_6E_2$	n = 3				None	0	-1.48±0.1
$K_3(QL)_6E_2RGDS$	n = 3				RGDS	+1	44.57±0.3
$K_3(QL)_6E_2YGFGG$	n = 3				YGFGG	+1	10.57±0.1

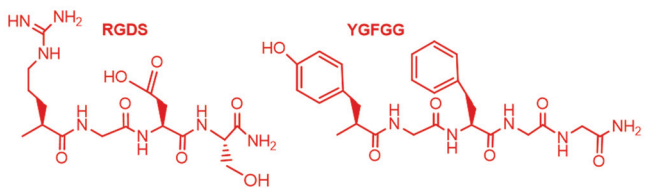

Fig. 1 Chemical structure of the multi-domain peptides (MDPs) designed for interfacial self-assembly with HA, their expected charge and zeta potential measured at neutral pH.

chemical motifs, the membranes can be made intrinsically bioactive not requiring post-functionalization. To tailor these membranes for bone regeneration applications, this work exploits MDPs functionalized with bioactive motifs derived from mineralizing[30] and cell adhesive (fibronectin, FN)[31] proteins and bone anabolic factors (osteogenic growth peptide, OGP)[32] to generate membranes with intrinsic mineralization capacity and cell-adhesive and osteoinductive properties. The presence of negatively charged glutamic acid residues (E_2)[33] at the C-terminal ($K_3(QL)_6E_2$) aims to attract and localize calcium ions at this flank of the peptide as a means to create a nucleation point for mineralization. The RGDS and YGFGG epitopes, derived respectively from FN and OGP, were also incorporated at the C-terminal of the MDPs. The RGDS domain is well known to be involved in cell adhesion through integrin-mediated processes.[31] The physiologically active form of OGP is obtained by proteolytic cleavage of the C-terminal (OGP [10–14], YGFGG)[34,35] and is known to interact with cell membrane receptors activating the MAP kinase, Src and RhoA signalling pathways.[36,37] OGP regulates cell proliferation, alkaline phosphate activity and matrix mineralization.[37] OGP[10–14] has shown to increase bone formation and trabecular bone density.[38,39] Thus, OGP and OGP[10–14] peptides have been chemically immobilized on surfaces by click chemistry or incorporated into self-assembling peptide gels to enhance osteogenic differentiation of MC3T3-E1 cells.[40,41] The osteogenic ability of this peptide could, for example, eliminate the need for exogenous supplementation of bone growth factors to promote osteogenic differentiation of stem cells. These biochemical signals were designed and selected to achieve an optimal cell microenvironment and maximize the osteogenic potential of the membrane.

Although the biochemical functionalities used in this work have been previously explored in other studies,[33,34,41–43] to the best of our knowledge they have never been presented in an interfacial self-assembled membrane. Furthermore, compared to previously developed HA–peptide membranes, the current system presents a more advanced design by adding multiple functionalities to the membrane for controlled and selective interactions. Thus, the goal of this work consists of the integration of selective and interactive molecular functionalities into the membrane formulation able to promote multiple biological outcomes for coordinated bone regeneration. The ability of the membranes to grow cells is evaluated using periosteum-derived cells (PDCs). PDCs were selected as the cell source due to their relative ease of isolation and higher proliferative rates than mesenchymal stem cells (MSCs).[44] Human PDCs show multipotency similar to human bone marrow cells (BMCs) as both types of cells originate from mesoderm-derived populations during embryonic development. Since PDCs are vital during fracture healing, this type of cell might be a more suitable cell population for bone engineering applications than the commonly used BMCs.[45] By testing the ability of these molecularly designed membranes to support the adhesion of PDCs, we expect to take a step closer to developing a functional periosteum graft.

2 Experimental

2.1 Peptide synthesis and purification

MDPs (Fig. 1) were synthesized in an automated peptide synthesizer (Liberty Blue, CEM, UK) using standard 9-fluorenylmethoxycarbonyl (Fmoc)-based solid phase chemistry. Rink Amide MBHA resin (100–200 mesh) was used for synthesizing $K_2(QL)_6K_2$, $K_2(SV)_6K_2$, $K_3(QL)_6E_2$RGDS and $K_3(QL)_6E_2$YGFGG, while Glu(O*t*Bu)-Wang resin (100–200 mesh) was used for the synthesis of $K_3(QL)_6E_2$. Amino acids were coupled using 4 mol equivalents of Fmoc protected amino acids, 4 mol equivalents of 1-hydroxybenzotriazole hydrate (HOBt) and 4 equivalents of *N*,*N*′-diisopropylcarbodiimide (DIC). Fmoc deprotections were achieved using 20% (v/v) piperidine in dimethylformamide (DMF). Before cleavage from the resin, the N-terminus of the peptides was acetylated using 10% (v/v) acetic anhydride in DMF. The acetylation reaction was carried out at room temperature under shaking in two cycles of 3 and 7 minutes, with an intermediate extensive washing with DMF. After washing several times with DMF and dichloromethane (DCM), a Kaiser test was performed to confirm acetylation (negative, no free amine groups). Peptide cleavage from the resin and the removal of the protecting groups were carried out with a mixture of trifluoroacetic acid (TFA)/triisopropylsilane (TIS)/water (95%/2.5%/2.5%) for 3 hours at room temperature. The peptide mixture was collected and the excess of TFA was removed using a rotary evaporator. The resulting viscous peptide solution was triturated with cold diethyl ether. The white precipitate was allowed to dry overnight after centrifugation and removal of the supernatant. The peptide mass was confirmed by electro-spray ionization mass spectrometry (ESI-MS) using a single quadrupole mass detector (SQ Detector 2, Waters, USA). Peptides were then purified using a Waters AutoPurification preparative scale high-performance liquid chromatography (HPLC) system equipped with a binary gradient (2545) module, UV/Vis (2489) and mass (SQD2) detectors, sample manager (2767) and a preparative reverse-phase C18 column (XBridge Prep 5 μm, OBD 30 × 150 mm, Waters, USA). Peptide samples were eluted at 20 mL min^{-1} in a water/acetonitrile (0.1% TFA) gradient. Fractions were collected based on the peptide mass, concentrated by rotary evaporation and then lyophilized. TFA counter-ions were exchanged by sublimation from 0.01 M hydrochloric acid or by solid phase extraction using PL-HCO_3 MP SPE columns (Agilent Technologies, USA). Finally, the peptides were dialysed against ultrapure water using 500 MWCO dialysis tubing, and subsequently lyophilized. Their purity was checked by analytical HPLC (Alliance HPLC system coupled with a 2489 UV/Vis detector, Waters, USA). Peptide solutions (1 mg mL^{-1}, 100 μL) were injected into an analytical reverse-phase C18 column (XBridge analytic 5 μm, 4.6 × 150 mm, Waters, USA) and eluted at 1 mL min^{-1} using a water/ACN (0.1% TFA) gradient with UV detection at 220 nm. The peptide mass was confirmed by MS as described above.

2.2 Peptide characterization

To determine the overall charge of MDPs at different pH values, the zeta potential of aqueous MDP solutions (0.1 wt%) was measured using a Zetasizer Nano ZS instrument (Malvern Instruments Ltd, UK). MDPs were dissolved at 0.1 wt% in ultrapure water and their pH was adjusted to 3, 7 and 9 with hydrochloric acid (0.1 M) or ammonium hydroxide (0.1 M). Peptide solutions were aged for 4 hours prior to the zeta-potential measurement. The samples were loaded into a U-shaped cuvette, equipped with gold electrodes, and the zeta potential was recorded at 25 °C.

The secondary structure of the MDPs was analysed by circular dichroism (CD) spectroscopy. Peptides were dissolved in deionized water to a final concentration of 0.011 mM and the pH was adjusted to 3, 7 and 9 with hydrochloric acid (0.1 M) or ammonium hydroxide (0.1 M). To study the influence of charge screening on the MDP conformation by the presence of counterions (*e.g.* phosphate ions), the peptides were also dissolved in a 3 mM phosphate solution to obtain 0.011 mM concentration and the pH was adjusted to 7. The CD signals of water and phosphate solution were also measured and subtracted from the CD signal obtained for the peptide solutions. The CD measurements were performed on a PiStar-180 spectrometer from Applied Photophysics (UK) under a constant flow of nitrogen (8 L min^{-1}) at a constant pressure value of 0.7 MPa. Far-UV spectra were recorded at 25 °C from 190 to 300 nm in a quartz cuvette with 1 mm path-length. All scans were performed in the steady state with a bandwidth of 1 nm and each presented spectrum is an average of 3 spectra. The molar ellipticity [θ] was then calculated ($[\theta] = \theta/(C \cdot l)$ where θ is the measured ellipticity in mdeg, C is the concentration of the peptide in dmol L^{-1} and l is the light path length of the cuvette in cm).

To gain further insights into the peptide secondary structure, attenuated total reflectance-Fourier transform infrared (ATR-FTIR) spectroscopy was performed on dried MDP films. For this, 5 μL of each MDP solution (1 wt%) in D_2O was deposited onto the "Golden Gate" diamond crystal ATR accessory (Specac, UK) and dried using a stream of nitrogen. Then, the spectrum was acquired in the absorbance mode using a FTIR spectrometer (Bruker TENSOR 27, Germany) in the range of 1750–1500 cm^{-1} by averaging 256 individual scans per peptide film at a resolution of 4 cm^{-1}. Collected spectra were linear baseline corrected, normalized, and subsequently deconvoluted by fitting with a mix Gaussian/Lorentzian function using PeakFit software.

To analyse the nanostructures formed by the new MDPs under different conditions, transmission electron microscopy (TEM) imaging was performed. Peptide solutions were prepared at 0.01 wt% in ultrapure water or 10 mM phosphate solution. Samples were observed under three different conditions: water at pH 7, phosphate solution at pH 7 and 11 adjusted with hydrochloric acid (0.1 M) or ammonium hydroxide (0.1 M). After being aged for 48 hours, the peptide solutions were loaded onto the carbon film coated copper girds (400 mesh, Agar Scientific, UK) and negatively stained by 2 wt% uranyl acetate (Agar Scientific, UK). The excess staining solution on the grids was removed with filter paper and the grids were allowed to dry at room temperature for at least 3 hours. Bright field TEM imaging was performed on a JEOL (Japan) 1230 TEM operated at an acceleration voltage of 100 kV and images were recorded by using a SIS Megaview III wide angle CCD camera.

2.3 Preparation of HA-MDP membranes

Peptide and HA solutions were prepared by dissolving the powders in ultra-pure water to obtain the desired concentration. The membranes were prepared in a sterile environment using a 96 well plate as a template. 50 μL of a 2% (w/v) HA (700 kDa, Lifecore Biomedical, USA) solution was cast at the bottom of the wells (Fig. 2A) and then 50 μL of 3% (w/v) peptide solution was added on top of the HA solution (Fig. 2B). The solutions were incubated at 60 °C for 4 hours (Fig. 2C) to accelerate the process of membrane formation, but membranes can also form at RT and 37 °C. The membranes

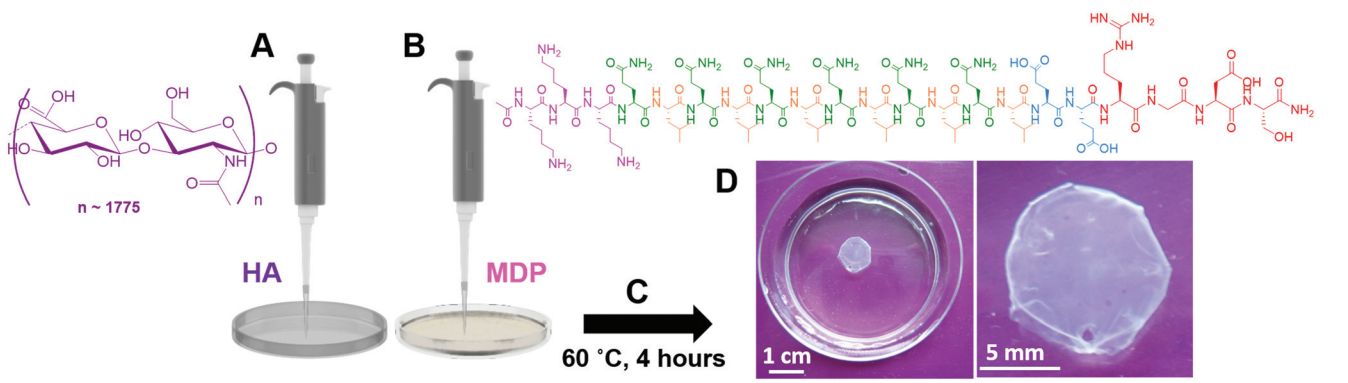

Fig. 2 Membrane fabrication by interfacial self-assembly. Membranes are formed by first casting the HA solution (A) followed by the addition of MDP solution (B) on top. A membrane immediately forms at the interface of both solutions which further develops into a robust membrane (D) after incubation at 60 °C for 4 hours (C).

were rinsed with sterile ultrapure water to remove unreacted HA and peptide (Fig. 2D).

2.3.1 Characterization of membrane microstructure. The microstructure of the membrane surface and cross-section was examined by scanning electron microscopy (SEM). For this, the membranes were prepared by immersion in 2% glutaraldehyde/3% sucrose in PBS for 1 hour at 4 °C. The membranes were then progressively dehydrated using graded ethanol concentrations. Ethanol removal was performed using a critical point dryer (EMS 850, Electron Microscopy Sciences, USA). All membrane samples were first coated with a gold layer (5–30 nm) using an Emitech SC7620 sputter coater (Quorum Technologies, UK) and then imaged using an ultra-high resolution field emission gun scanning electron microscope (FEG SEM, Inspect F50, FEI, The Netherlands).

2.3.2 Membrane mineralization. Membranes formed with $K_2(QL)_6K_2$, $K_3(QL)_6E_2$, $K_3(QL)_6E_2RGDS$ and $K_3(QL)_6E_2YGFGG$ were used for the mineralization studies. The membranes were incubated in a modified stimulated body fluid (m-SBF) solution, prepared as described previously,[46] for 7, 14 and 21 days at 37 °C under sterile conditions. The m-SBF solution is 1.5× concentrated and contains ion concentrations (Na^+ 142.0, K^+ 5.0, Ca^{2+} 2.5, Mg^{2+} 1.5, Cl^- 103.0, HCO_3^- 10, HPO_4^{2-} 1.0, SO_4^{2-} 0.5 mM) nearly equal to those of human blood plasma.[47,48] m-SBF solution was renewed twice a week and coverslips were used as the control substrate. After each immersion time, the membranes were removed from m-SBF, washed with distilled water and prepared for SEM observation. Membranes were first dehydrated using graded ethanol concentrations and ethanol removal was performed using a critical point dryer (CPD, Autosamdri-815 Series A, Tousimis, USA). To evaluate membrane mineralization, the membranes were analysed by using a high-resolution field emission SEM (AURIGA Compact, Zeiss, Germany) equipped with energy dispersive electron X-ray (EDX) spectroscopy (Bruker QUANTAX ESPIRIT 2.0 EDS system, X-flash detector, Germany). For the EDX analysis, the membranes were coated with carbon by thread evaporation. EDX measurements were carried out at an accelerating voltage of 10.0 kV and a working distance of 8 mm to identify the chemical composition of the mineral formed on the membrane surface. The atomic percentage of calcium and phosphorus was determined using ESPIRIT 2.0 software (Bruker, Germany) from which the calcium-to-phosphorus ratios were calculated. For SEM examination, the membranes were coated with platinum by ion sputtering (EM ACE600, Leica, Germany).

2.4 Cell adhesion assay

2.4.1 Isolation and culture of periosteum derived cells (PDCs). PDCs were isolated from human periosteum samples obtained from patients with open fractures, under the framework of an agreement with the Hospital of Guimarães (Portugal), approved by the ethical committees of both institutions and after informed consent by the patients. The explants were rinsed with PBS supplemented with 2% of antibiotic, placed in culture flasks and cultured in alpha minimum essential medium Eagle (alpha-MEM), containing 10% fetal bovine serum (FBS) and 1% antibiotic, for two weeks until cells became confluent. Medium was renewed twice a week. After reaching confluence, the cells were trypsinized and expanded up to passage 5. The expanded cells were subjected to flow cytometry analysis to assess the mesenchymal nature of PDCs (Fig. S10†). The cells were detached using TryPLE Express (Thermo Fisher, USA), washed in PBS and centrifuged at 300*g* for 5 minutes. The resulting pellet was resuspended in cold PBS with 1% FBS. Different aliquots of the cell suspension were mixed with mouse anti-human CD105-FITC (AbD Serotec, USA), CD90-APC (eBioscience, USA), CD73-PE, CD45-FITC, CD34-PE (all from BD Biosciences, USA) and CD31-APC (R&D Systems, USA) using the manufacturer's protocols. After 20 minutes of incubation at room temperature in the dark, the cells were washed with PBS and centrifuged at 300*g* for 5 minutes. After discarding the supernatant, the cells were resuspended in 1% formalin in PBS and analyzed using a FACSCalibur flow cytometer (BD Biosciences, USA). The results were analysed using Cyflogic software (1.2.1, CyFlo Ltd, Finland).

2.4.2 PDC seeding and culture on MDP-coated coverslips and HA-MDP membranes. To determine the effect of the MDPs alone on PDCs, cells were first cultured on MDP-coated surfaces and then directly on HA-MDP membranes. The MDPs were dissolved in sterile ultra-pure water at 0.01 wt% and sterilized by UV exposure for 15 minutes. 100 μL of peptide solution was placed in the centre of the coverslip (6.35 mm tissue culture coverslips, made of polyethylene terephthalate and glycol-modified (PET-G), Sarstedt AG & Co, Germany) and allowed to evaporate overnight in a sterile tissue culture hood. To produce sterile HA-MDP membranes, HA was sterilized by dissolving the polymer in water followed by filtration through a 0.22 μm filter and lyophilisation in sterile Falcon tubes (Sartorius, USA). Membranes were prepared as previously described. PDCs at passages 3–4 were harvested from culture flasks using trypLE Express (Thermo Fisher, USA). Cells were washed with PBS and centrifuged at 200*g* for 5 minutes. The cell pellet was resuspended in serum-free DMEM (without phenol red) and the cells were seeded at 10 000 cells per coverslip or HA-MDP membrane (peptide side), both previously placed into wells of a 96 well plate. The cells were then cultured at 37 °C in a humidified atmosphere of 5% CO_2 for 2, 14 and 24 hours.

2.4.3 Cell morphology on coverslips and HA-MDP membranes. To investigate the morphology of adherent PDCs cultured on MDP-coated coverslips and HA-MDP membranes, F-actin and nuclei staining was performed. After 2, 14 and 24 hours, the culture medium was removed and the samples were washed twice with PBS to remove any non-adherent cells. The attached PDCs were fixed using a 10% formalin solution for 30 minutes at 4 °C. The membranes were then washed with 0.1 M glycine in PBS and twice with PBS. For cell permeabilization, a 2% BSA/0.2% Triton X-100 solution was used for 1 hour at RT. 4,6-Diamidino-2-phenylindole-dilactate (DAPI) and phalloidintetramethylrhodamine B isothiocyanate dyes (phalloidin) were used to stain the cell nuclei and F-actin fila-

ments, respectively. Briefly, for each time point, 1 mL of PBS containing 10 μL of phalloidin-TRITC was added to each coverslip for 1 hour at room temperature and protected from light. After extensive washing, samples were stained with 1 μL of DAPI in 1 mL of PBS for 30 minutes. After DAPI staining, the membranes were washed three times with PBS. Cells cultured on the membranes were visualized using a Leica TCS SP8 inverted confocal microscope (Leica, Germany) while cells on coverslips were observed using a Zeiss axio observer fluorescence inverted microscope (Zeiss, Germany). The images were then processed and analysed using Fiji ImageJ software (http://fiji.sc/, ROI manager tool) to quantify cell morphology (cell area and aspect ratio). Ten cells were randomly selected from each image (in a total of three images per condition) and their perimeters demarcated. Cells were fitted to an ellipse and then the cell area (selected area in μm^2) and aspect ratio (AR, ratio between the major and minor axes of the ellipse) were calculated. The morphology of the cells and interaction with the membranes were also examined by SEM. For this, cell cultured membranes were fixed, dehydrated and prepared as described in section 2.3.2.

2.4.4 Cell numbers (DNA quantification and cell density) on MDP-coated coverslips and HA-MDP membranes. The number of cells attached onto MDP-coated coverslips and membranes was estimated by DNA quantification using a fluorimetric double-strand DNA quantification kit (PicoGreen, Molecular Probes, Invitrogen, UK). For this purpose, cells were collected at 2, 14 and 24 hours by transferring the cell cultured coverslips or membranes into 1.5 mL microtubes containing 1 mL of ultrapure water The samples were subjected to freezing/thawing cycles to lyse cells and were then stored in a −80 °C freezer until DNA quantification. Samples were thawed and sonicated for 15 minutes. Samples and standards (ranging from 0 to 2 mg mL^{-1}) were mixed with a PicoGreen solution according to the manufacturer's instructions in an opaque 96-well plate. Three replicates were prepared for each sample and standard. The plate was incubated for 10 minutes in the dark and fluorescence was measured in a microplate ELISA reader (BioTek, USA) with an excitation of 485/20 nm and an emission of 528/20 nm. A standard curve was created and DNA values were calculated from the calibration curve for each culture condition. Cell density (number of cells per mm^2) was also calculated by counting the number of DAPI stained nuclei in the captured image area (0.34 mm^2) using Fiji ImageJ. Three images per condition were used for the quantification.

2.5 Statistical analysis

EDX analysis and cell culture assays were performed in triplicate. The zeta-potential values, Ca/P ratios and DNA quantification values are presented as mean ± standard deviation (SD). Statistical analysis was performed using GraphPad Prism 5 software (USA). Statistical differences in DNA quantification were determined using a two-way analysis of variance (ANOVA) with a Bonferroni's multiple comparison *post-hoc* test ($^*p < 0.05$; $^{**}p < 0.01$; $^{***}p < 0.001$).

3 Results and discussion

3.1 Peptide design for membrane self-assembly and bioactivity

In this work, we have redesigned MDPs to contain a positively charged block, composed of multiple lysine residues (K_2 and K_3) at the N-terminal, and a positively or negatively charged block (K_2 or E_2) at the C-terminal, while keeping a similar design of alternating hydrophilic (Q or S) and hydrophobic aliphatic residues (L or V) in the central block (Fig. 1). The presence of positively charged lysine at both termini ($K_2(QL)_6K_2$ – control, and $K_2(SV)_6K_2$) is expected to promote electrostatic interactions with HA, known to be required for the self-assembly of stable membranes. The hydrophobic residue leucine (L, $K_2(QL)_6K_2$) was replaced by valine (V, $K_2(SV)_6K_2$) and the hydrophilic glutamine (Q, $K_2(QL)_6K_2$) by serine (S, $K_2(SV)_6K_2$) in order to investigate the effect of these amino acids in the peptide self-assembly, since both Val and Ser are known to have higher propensity for β-sheet formation than Leu and Gln, respectively.[49]

All MDPs listed in Fig. 1 were successfully synthesized and purified, as confirmed by ESI-MS and HPLC analysis (Fig. S1–S5†). Taking into account the importance of the electrical charge on the self-assembly of MDPs, the zeta potential of peptide solutions was measured at different pH values (Table S2†). At neutral pH, all MDPs show positive values of zeta potential, except $K_3(QL)_6E_2$ (Fig. 1) which has a slightly negative zeta potential. The expected charge of this MDP at pH 7 is zero due to the free carboxylate at the C-terminal.

3.2 Self-assembly behaviour of MDPs

Previous studies[24,26,27] reported that MDPs were able to form β-sheet secondary structures. However, in the current study additional amino acids were introduced in the original design, which are expected to affect the balance of molecular interactions. CD analysis of MDP solutions revealed the presence of β-sheet secondary structures at neutral pH for MDPs $K_3(QL)_6E_2$, $K_3(QL)_6E_2RGDS$ and $K_3(QL)_6E_2YGFGG$ (Fig. 3A), while at basic pH all MDPs exhibit a β-sheet conformation (Fig. S6†) with zero ellipticity around 200–210 nm, a minimum peak at 217–218 nm and positive maximum at 194–198 nm. The presence of oppositely charged residues at both termini in MDPs $K_3(QL)_6E_2$, $K_3(QL)_6E_2RGDS$ and $K_3(QL)_6E_2YGFGG$ at pH 7, may promote their dimerization into an antiparallel β-sheet arrangement due to attractive electrostatic interactions among individual peptide monomers without the addition of any trigger. ATR-FTIR analysis (Fig. 3B) was then performed to infer about the β-sheet arrangement. It has been shown that most MDPs tend to organize into antiparallel β-sheets.[24,25,27] All spectra exhibited a strong absorbance between 1610 and 1630 cm^{-1}, corresponding to parallel amide (Amide $I_{\parallel}$) and indicative of an extended amyloid-like β-sheet, thus supporting the CD results. All MDPs also showed a peak at ~1695 cm^{-1} characteristic of perpendicular amide (Amide $I_{\perp}$) suggesting that the β-sheets are anti-parallel. In $K_2(QL)_6K_2$, $K_3(QL)_6E_2$, $K_3(QL)_6E_2RGDS$ and $K_3(QL)_6E_2YGFGG$ peptides, the peak at

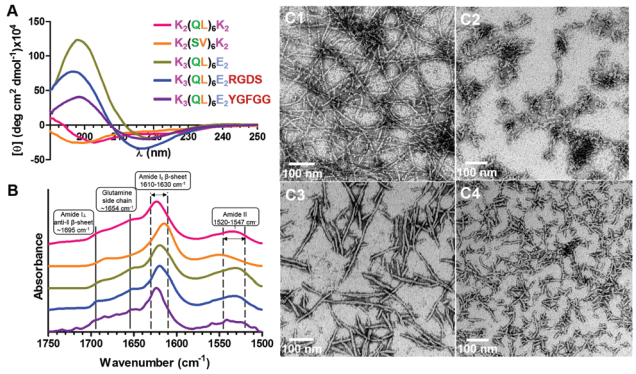

Fig. 3 (A) CD spectra of the synthesised MDPs at 0.011 mM in water (pH 7); (B) ATR-FTIR spectra of MDP dried films (1 wt%) showing the characteristic peaks (1695, 1650, 1616 and 1526 cm^{-1}). Spectra were baseline corrected, normalized and stacked for clarity. (C) TEM images of MDP assemblies (0.01 wt%, pH 7), (C1) $K_2(QL)_6K_2$; (C2) $K_3(QL)_6E2$; (C3) $K_3(QL)_6E2RGDS$; (C4) $K_3(QL)_6E2YGFGG$.

1650 cm^{-1} from glutamine side chains is also observed. The FTIR spectra were further deconvoluted and the observed positions are described in Fig. S7.† It has been demonstrated that β-sheet conformation is crucial to promote the self-assembly of peptides into nanofibers.[50–52] To assess the morphology of peptide assemblies, TEM was carried out under different conditions (Fig. 3C and 4B). At pH 7, $K_2(QL)_6K_2$ showed a dense network of long fibres (Fig. 3C1), but surprisingly no aggregates were observed for $K_2(SV)_6K_2$ using TEM performed under similar conditions. A similar MDP ($K_2(SL)_6K_2$) was shown to form long nanofibres,[25] as observed by cryo-TEM. Based on these prior observations, and the fact that the only difference between these MDPs is the presence of valine (V) instead of leucine (L), one can speculate that the lower hydrophobicity of valine may delay the initial dimerization (formation of the "hydrophobic sandwich"),[25] especially when this MDP is highly charged at pH 7 (Table S2†). Hydrophobicity can be expressed as the logarithm of octanol/water partition coefficient, log *P*. Using the tool for calculating properties of molecules in the Molinspiration Cheminformatics software,[53] the milog *P* of Val and Leu were calculated to be −1.91 and −1.38, respectively, confirming the lower hydrophobicity of Val (the higher the log *P*, the more hydrophobic the molecule). $K_3(QL)_6E_2$ formed short aggregates with a rod-like morphology (Fig. 3C2), while the presence of RGDS seemed to promote the elongation of the aggregates into fibres of intermediate length (Fig. 3C3). TEM of $K_3(QL)_6E_2YGFGG$ showed the presence of short nanofibres with uniform length (Fig. 3C4). The differences in nanofibre length exhibited by these MDPs might have resulted from the fine balance between hydrophobic and electrostatic interactions among peptide molecules, as they present distinct zeta potential at neutral pH (Table S2†).

To test the effect of charge screening by the addition of counter-ions (*e.g.* PO_4^{3-}), the MDPs were dissolved in a 10 mM phosphate solution. In the presence of phosphate ions, $K_2(QL)_6K_2$ and $K_2(SV)_6K_2$ showed typical spectra of a β-sheet conformation. Moreover, the CD signal for the other MDPs was reinforced as observed by an increase in the maximum at around 197 nm and a simultaneous decrease at 218 nm (Fig. 4A). The presence of phosphate seemed to promote the aggregation of the nanofibres, as seen in the TEM analysis (Fig. 4B). Under these conditions, TEM of $K_2(SV)_6K_2$ showed bundles of aggregates with an irregular morphology (Fig. 4B2). At basic pH (pH 11) and in the presence of 10 mM phosphate (Fig. S8†), MDPs $K_3(QL)_6E_2$, $K_3(QL)_6E_2RGDS$ and $K_3(QL)_6E_2YGFGG$ formed well-defined nanofibre structures of different lengths (as seen at pH 7, Fig. 4B), while for $K_2(QL)_6K_2$ entangled fibres were observed. Surprisingly, $K_2(SV)_6K_2$ showed irregular aggregates with a fibre-like morphology. Phosphate ions promote ionic crosslinking between amines of lysine residues favouring self-assembly, nanofibre growth and entanglement. The same behaviour has been observed with other MDPs reported in the literature.[25,27]

3.3 Fabrication of self-assembled membranes displaying different functionalities

The self-assembly of $K_2(QL)_6K_2$ and HA into membranes was previously reported.[23] Moreover, the incorporation of the cell-adhesive sequence RGDS at the C-terminal promoted the adhesion and spreading of rat MSCs on the membranes. Inspired by this work, and aiming at expanding the biofunctionality of these membranes, the membranes were fabricated through interfacial self-assembly combining HA and MDPs (Fig. 2) with different bioactive motifs. The self-assembly process generates membranes with distinct faces, one rich in HA (bottom side) and the other containing the peptide (top side). SEM images of the overall membrane structure (Fig. S9†) did not show noticeable macroscopic differences.

However, microscopic examination of the membrane cross-section and top surface (Fig. 5) revealed differences in their structural organization and surface nanotopography. Previous studies combining HA and peptide amphiphiles showed the formation of a highly organized structure composed of two distinct surfaces, one showing a rough and amorphous morphology corresponding to the HA side and the other exhibiting

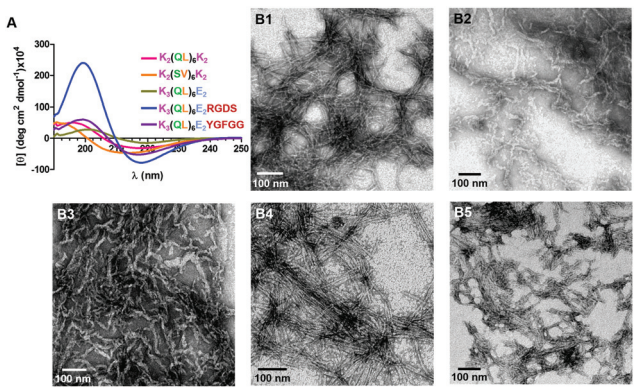

Fig. 4 (A) CD spectra and (B) TEM images of MDPs in phosphate solutions (pH 7) at 0.011 mM and 0.01 wt% concentration, respectively. (B1) $K_2(QL)_6K_2$; (B2) $K_2(SV)_6K_2$; (B3) $K_3(QL)_6E_2$; (B4) $K_3(QL)_6E_2RGDS$; (B5) $K_3(QL)_6E_2YGFGG$.

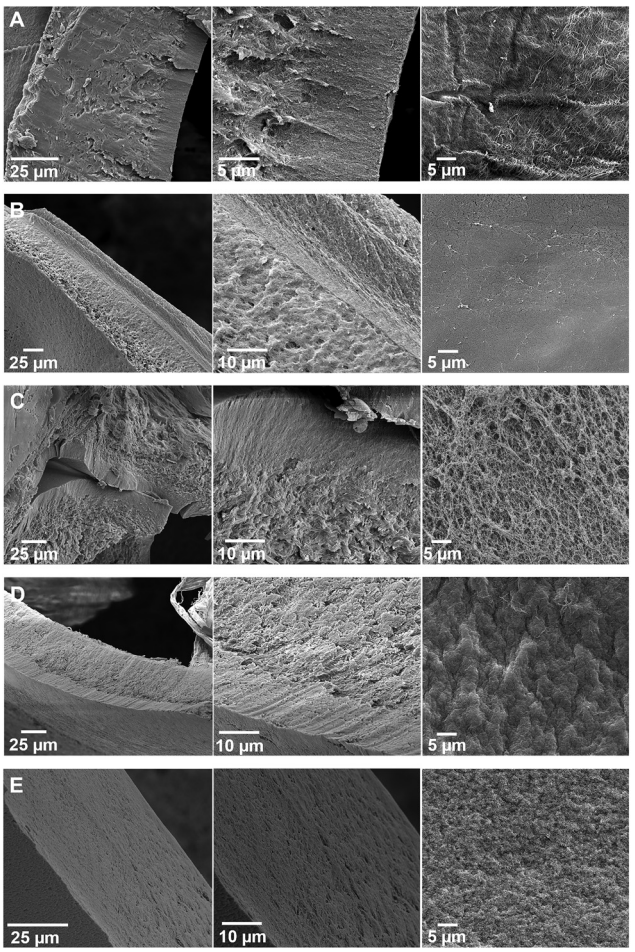

Fig. 5 SEM micrographs of the self-assembled HA-MDP membranes showing the cross-section (left and central panels) and surface (peptide side, right panel). (A) $K_2(QL)_6K_2$, (B) $K_2(SV)_6K_2$, (C) $K_3(QL)_6E_2$, (D) $K_3(QL)_6E_2$RGDS and (E) $K_3(QL)_6E_2$YGFGG.

randomly distributed nanofibers similar to the fibrillar structure of natural ECM,[15,17,23] assigned to the peptide side. With the exception of the membrane formed with $K_3(QL)_6E_2$YGFGG, the cross section of all other membranes showed layers with distinct fibre organization. Fibres tended to align closer to the interface which then became less organized in the inner part (contact with HA). When the central block was composed of alternating serine and valine ($(SV)_6$), a parallel fibre arrangement near the interface was observed when compared with the membrane obtained with control MDP ($K_2(QL)_6K_2$). Such behaviour suggests that the primary sequence of the MDPs affected the interaction with HA and consequently the membrane structural organization. The membrane obtained with $K_3(QL)_6E_2$YGFGG showed a homogeneous structure with indistinguishable layers. This amorphous organization was consistently observed for this membrane. Although this result is not fully understood, the presence of an aromatic/hydrophobic sequence (YGFGG) at the C-terminal of this MDP may have an effect on how it behaves at the air–liquid interface, resulting in a membrane with a different microscopic organization. Depending on the MDP used, the surface of the membranes also showed differences in terms of nanotopography, reflecting the morphology of the peptide assemblies seen using TEM. The surface of the membrane formed with $K_2(QL)_6K_2$ showed a dense network of long nanofibers, whereas the ones formed with $K_2(SV)_6K_2$ and $K_3(QL)_6E_2$YGFGG exhibited a compact structure without the presence of well-defined fibres. Membranes made with RGDS-containing MDP showed surface topography similar to the control membrane, but the observed nanofibres are shorter. In contrast to the other membranes, the surface of the membrane obtained with MDP $K_3(QL)_6E_2$ is less compact, showing a more porous structure formed of entangled fine nanofibres. Considering that the membrane formed with $K_2(SV)_6K_2$ MDP did not show a nanofibrillar surface, we have focussed the following studies on the other membranes and using the membrane formed with $K_2(QL)_6K_2$ as a control.

3.4 *In vitro* membrane mineralization

It is known that the proteins involved in the mineralization *in vivo* are often highly acidic, promoting supersaturation of calcium ions necessary for the nucleation of calcium phosphate (CaP) minerals.[30,33,54] For example, it has been shown that negatively charged surfaces promote mineralization[54] and that the presence of carboxyl groups enhances CaP nucleation.[55] In this study, we included glutamic acid residues in the $K_3(QL)_6E_2$ peptide to attract calcium ions through complexation with carboxylate groups on their side chains, leading to the nucleation and growth of CaP. This residue has been used to promote oriented mineralization on a supramolecular peptide amphiphile template.[33]

To assess the mineralizing ability of the membranes, an m-SBF solution was used.[46] The ion concentration of this solution is 1.5-fold higher than in the normal SBF and is typically used to accelerate the mineralization process. The SEM images of the membranes after incubation in SBF for 21 days (Fig. 6) revealed the formation of CaP mineral with a hemispherical morphology. The control surface (glass coverslip) did not show deposition of CaP minerals (data not shown). For the membranes formed with $K_3(QL)_6E_2$YGFGG, a few CaP nuclei were detected on the membrane, while in the other membranes more CaP minerals were observed. The chemical composition of the mineral formed on the membrane was then analyzed by EDX, which confirmed the presence of calcium and phosphorus elements (Fig. 6). The Ca/P ratios obtained for the membranes formed with MDP $K_2(QL)_6K_2$, $K_3(QL)_6E_2$, and $K_3(QL)_6E_2$RGDS were within the range previously designed for precipitated hydroxyapatite ($Ca_{10}(PO_4)_6(OH)_2$) between 1.33 and 1.67. Mineral formed on the $K_2(QL)_6K_2$ membrane showed a Ca/P ratio equal to 1.5, typical of α- and β-tricalcium phosphate ($Ca_3(PO_4)_2$).[56] Since this MDP does not contain carboxylate groups, the mechanism for mineral formation may have first occurred through electrostatic interactions between positively charged amine groups (NH_3^+) of lysine (K) residues and phosphate ions (PO_4^{3-}) in the mineralizing solution and their subsequent complexation with Ca^{2+}. For the membranes made with $K_3(QL)_6E_2$YGFGG, the

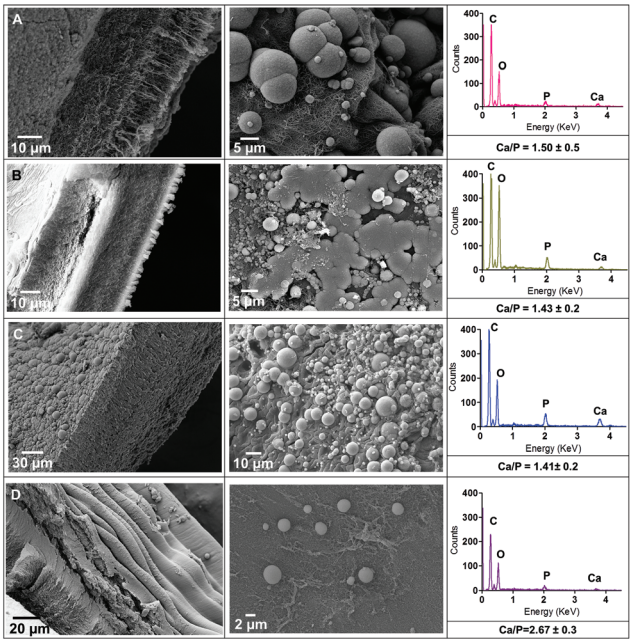

Fig. 6 SEM micrographs and EDX analysis of the surface (peptide side) of self-assembled membranes after immersion in SBF for 21 days. (A) $K_2(QL)_6K_2$, (B) $K_3(QL)_6E_2$, (C) $K_3(QL)_6E_2RGDS$ and (D) $K_3(QL)_6E_2YGFGG$.

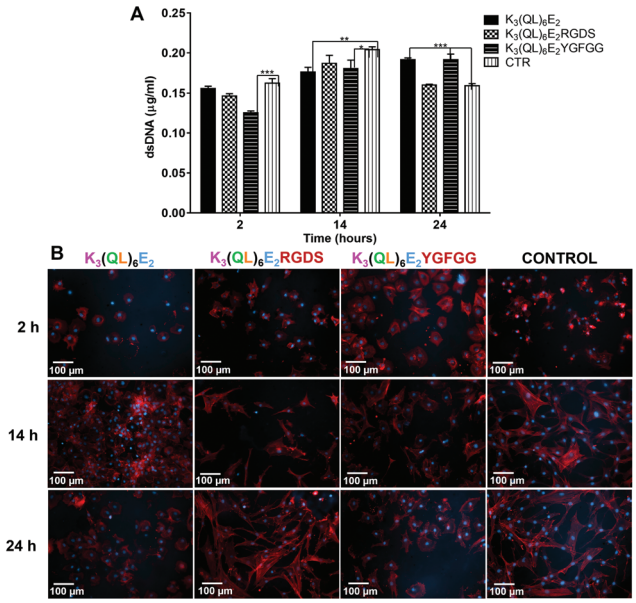

Fig. 7 Cell adhesion on uncoated (control) coverslips and coated with MDPs under serum-free conditions. (A) dsDNA quantification (***$p < 0.001$; **$p < 0.01$; *$p < 0.05$), error bars represent standard deviation. (B) Fluorescence microscopy images showing DAPI–phalloidin staining of PDCs cultured for 2, 14 and 24 hours. Cell nuclei were stained blue by DAPI and F-actin filaments in red by phalloidin.

ratio was 2.67, meaning that there was a higher deposition of calcium than phosphate ions, not leading to the formation of a desired CaP mineral.

3.5 *In vitro* cell adhesion

Studies investigating cell attachment on biomaterials typically use medium supplemented with animal-derived serum. Since the protein content of serum is poorly defined and protein adsorption could potentially mask the effect of the chemical signals displayed on the MDPs, serum-free conditions were used in this study. Before culturing cells on the membranes, a preliminary adhesion study was performed for 24 hours using PDCs cultured on coverslips coated with MDPs bearing the selected functionalities. The results indicated that PDCs were able to attach (Fig. 7) to the peptide-coated coverslips, as well as onto the control surface (uncoated coverslips).

DNA quantification results (Fig. 7A) showed that PDCs attach to the coverslips coated with the MDPs in similar quantities to the control during the first 2 hours, except in the presence of the OGP[10–14] pentapeptide. After 14 hours, similar DNA amounts were observed under all conditions, even though the control revealed higher DNA quantity. Under serum-free conditions, we should not expect a significant cell proliferation within 24 hours, therefore explaining the decrease in DNA quantity for the control and RGDS surface between 14 and 24 hours. However, the cells seeded on coverslips coated with the other MDPs were able to increase the cell numbers up to 24 hours. To further quantify cell adhesion on MDP-coated coverslips, cell density was calculated (Fig. S11A†). At 2 hours of culture, the number of cells adhered to the coverslip is significantly higher on the RGDS-MDP-coated coverslip, while at 24 hours the number of cells is significantly higher for $K_3(QL)_6E_2$, which is in accordance with the DNA quantification results. The fluorescence microscopy images (Fig. 7B) showed cells with different morphologies depending on the underlying substrate. Coverslips were coated with MDPs at a concentration of 0.01 wt%, the same concentration used for the TEM analysis. The differences in the size of the aggregates observed in the TEM (Fig. 2C) may explain the morphology of the cells on the coverslips. Cells became elongated after 14 hours for the control surface and surface coated with MDP containing the RGDS sequence, while the cells on surfaces coated with $K_3(QL)_6E_2$ and $K_3(QL)_6E_2YGFGG$ cells remained more round throughout the 24 hours of culture. This is confirmed by the analysis of the cell aspect ratio (AR, Fig. S11C†). Cells on $K_3(QL)_6E_2$ and $K_3(QL)_6E_2YGFGG$ surfaces exhibited lower ARs (1.46 ± 0.14 and 1.88 ± 0.58, respectively) at 24 hours, while on RGDS-MDP-coated coverslips and control surfaces PDCs have higher AR (3.03 ± 0.37), confirming the observed elongated morphology. An increase in the cell area from 2 to 24 hours is also observed for cells cultured on these two surfaces (Fig. S11B†), revealing increased cell spreading over time. By contrast, cells on the $K_3(QL)_6E_2$ and $K_3(QL)_6E_2YGFGG$ surfaces are more spread 2 hours after seeding and maintain their spread morphology at 24 hours. TEM images of $K_3(QL)_6E_2$ and $K_3(QL)_6E_2YGFGG$ showed short aggregates, while RGDS-containing MDP forms longer fibers. Cells may adapt their morphology according to the surface nanotopography, suggesting that PDCs seemed to

recognize the nanostructural features formed by the different MDPs. Despite these differences in the size of the assemblies formed by the various peptides, the surface chemistry (charge, hydrophobicity) may also have influenced the morphology of the attached cells. However, in this preliminary cell adhesion assay, it is not clear which factor contributes to the cell morphology, as it was not possible to decouple the chemical and physical features presented by the peptide assemblies. Several studies have shown that cells develop an elongated and flatter morphology on stiff substrates, than when cultured on soft surfaces.[57,58] When culturing cells on rigid substrates, such as coverslips, they generate more traction forces and typically exhibit pronounced actin stress fibres. While this has been observed for the control and RGDS-MDP-coated coverslip, the other two MDPs seemed not to favor this behavior.

To present the bioactive epitopes displayed on the MDPs to cells in a more physiologically relevant physical environment, membranes were fabricated by self-assembly using HA and MDPs. PDCs were seeded and cultured on these membranes under serum-free conditions. No cell proliferation was observed from 14 to 24 hours when PDCs were cultured on soft HA-MDP membranes. DNA quantification results (Fig. 8A) showed that when seeded on OGP[10–14]-containing membranes, PDCs were significantly higher in number than under the other conditions for all time points, also confirmed by cell density analysis (Fig. S11D†). Despite a small number of cells was found attached to the RGDS membrane, contrary to what was expected, the cells clearly exhibited a more extended morphology with focal adhesions, suggesting a distinct interaction with the membrane. These results suggest that the presence of OGP[10–14] pentapeptide enhanced the adhesion or survival of PDCs on the membranes. It has been shown that OGP [10–14] regulated cell proliferation and had a positive impact on cell numbers for osteoblastic-like cells.[37,59] Although our studies indicate that OGP[10–14] leads to enhanced cell adhesion under serum-free conditions, further and more detailed studies are needed to fully understand this effect. Cell morphology and distribution on the membranes were analyzed by confocal microscopy (Fig. 8B). Under all three conditions, PDCs were found to adhere throughout the membranes. After 24 hours, the PDCs cultured in the presence of RGDS presented a more elongated morphology in comparison with the other conditions. The quantification of cell morphology (Fig. S11E and F†) showed that PDCs cultured on membranes containing the $K_3(QL)_6E_2YGFGG$ MDP are initially more spread than on the other membranes, as measured by higher cell area, but at 24 hours cells on $K_3(QL)_6E_2$ exhibited an increased cell area. Although cells on the RGDS-containing membrane showed a lower area at 24 hours, their AR is significantly higher (2.76 ± 0.40), indicating a more elongated morphology. This might be related to differences in the microstructure of the membrane surfaces (Fig. 5C–E). The surface of the membrane formed with RGDS-containing MDP showed compacted nanofibers, whereas a more loose nanofibre network was observed in the membrane without a bioactive sequence and a relatively smooth surface for the membrane containing the OGP-derived pentapeptide. In addition, the presence of RGDS is expected to promote integrin binding that induces changes in the cytoskeletal organization.[60] Differences in cell morphology were also observed previously, when rat MSCs were cultured on the HA side of the membrane, as compared to the peptide side containing the RGDS sequence.[23] When cultured on the HA face, there were less cells attached exhibiting a rounded morphology. The less elongated cell morphology observed on the membranes, compared to coverslip substrates, is somehow expected, considering their softness. The morphology of PDCs was further examined by SEM (Fig. 9). Under

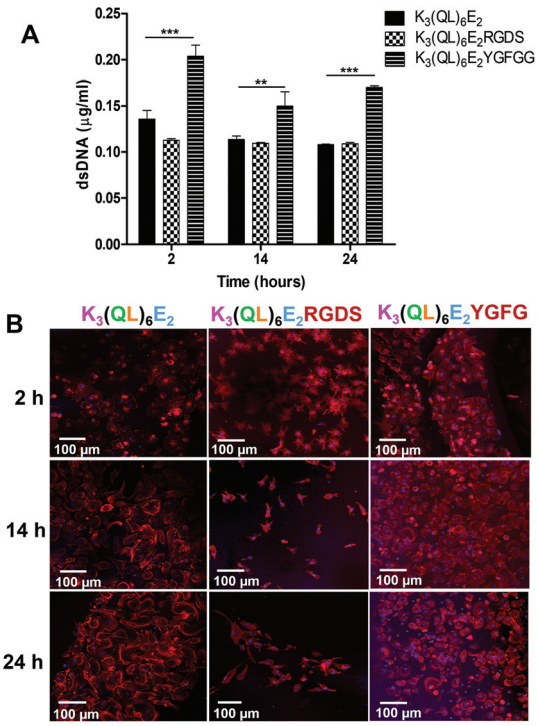

Fig. 8 Cell adhesion on HA-MDP membranes under serum-free conditions. (A) dsDNA quantification (***$p < 0.001$; **$p < 0.01$), error bars represent standard deviation. (B) Confocal microscopy images showing DAPI–phalloidin staining of PDCs cultured on the membrane surface (peptide side) at 2, 14 and 24 hours. Cell nuclei were stained blue by DAPI and F-actin filaments in red by phalloidin.

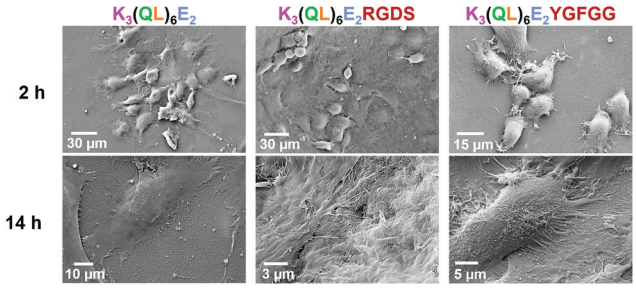

Fig. 9 SEM images showing PDCs on the surface of HA-MDP self-assembled membranes (peptide side) after 2 and 14 hours of culture under serum-free conditions.

all conditions, PDCs were seen to adhere to the membrane surface 2 hours post-seeding, exhibiting numerous pseudopodia and suggesting enhanced and stable adhesion to the membranes. After 14 hours, the PDCs cultured on membranes with $K_3(QL)_6E_2$ and $K_3(QL)_6E_2$RGDS were more flat, showing extended lamellipodia and filopodia and close interactions with the membrane surface. On the membranes formed with YGFGG-containing MDP, the cells were not fully extended, which might be due to the smoothness of the membrane surface. Collectively, the results showed good cell adhesion and interactions with the membrane surfaces under serum-free conditions. In addition to cell attachment, cell culturing substrates should also support the proliferation and spreading of attached cells. To assess cell proliferation on the membranes, cells were cultured in the presence of serum up to 14 days (Fig. S12†). These assays showed similar proliferation rates on the different membranes, with slightly higher proliferation for the OGP[10–14]-containing membranes (Fig. S12A†). Previous studies using OGP, immobilized on solid substrates[41] or incorporated into self-assembling peptide gels,[40] showed increased proliferation of pre-osteoblast cells (C3 T3-E1). The low proliferation rate seen for PDCs on the HA-MDP from day 7 to day 14 may indicate a transition from a proliferative phase to an early differentiation. SEM images at day 14 (Fig. S12B†) showed numerous cells adhered to the membrane surface, confirming that cells remained attached and spread on the membrane, but not in a confluent cell layer.

In this study, MDPs bearing different functionalities were used to co-assemble with HA, but future work should investigate variations in the density of these functionalities on the membrane to determine optimal cell responses, as shown in previous studies. For example, when incorporating the laminin-derived epitope (IKVAV) into a peptide amphiphile at different molar ratios (100 : 0, 90 : 10, 50 : 50, 40 : 60, and 10 : 90), the percentage of neural progenitor cells that differentiated into neurons was superior when the density of bioactive epitope was higher than 40%.[61] Nonetheless, the results from the cell adhesion and proliferation assays on the membranes suggest their potential in bone tissue engineering applications. These membranes can serve as scaffolds for the attachment and growth of PDCs and then be implanted *in vivo* to promote bone regeneration. Tejeda-Montes *et al.*[62] implanted thin elastin-based membranes, functionalized with mineralizing sequences derived from the statherin protein, into a 5 mm critical-size rat calvarial defect model and showed increased bone volume within the defect after 36 days after implantation. The membranes reported here could also be tested in a similar set-up, with or without cells attached, and potentially be used as barrier membranes in guided bone regeneration (GBR). According to a recent review on GBR,[63] the resorbable membranes used in this oral surgical procedure are typically made of synthetic copolymers of polylactide and polyglycolide (PLGA) or collagen. These membranes present several limitations, such as inflammatory reaction caused by acidic degradation products of PLGA and need for chemical crosslinking to improve collagen stability. In addition, they do not present functional organization or selective bioactivity. By contrast, the membranes reported here present a nanostructured organization with defined biochemical functionalities, while maintaining mechanical integrity *in vitro* in a physiological-like environment (up to 21 days) without the need for chemical crosslinking.

4 Conclusions

Novel self-assembled membranes were fabricated by combining negatively charged hyaluronan and multi-domain peptides containing different functionalities designed to promote bone regeneration. All the developed membranes showed intrinsic mineralizing capacity and the incorporation of different functionalities in the MDP sequence affected the microstructural organization of the membranes. The *in vitro* cell culture showed that the membranes were able to support the adhesion of primary human periosteal cells under serum-free conditions. These results indicate the potential of these membranes to deliver specific cell populations *in vivo*. The fabrication method (self-assembly) and water solubility of the building blocks allow the incorporation of cells during the membrane fabrication. The integration of multiple and specific biochemical signals in these nanostructured membranes can provide synergistic signalling to cells, stimulating their growth and differentiation and ultimately be used in bone regeneration applications. In addition, these membranes can be assembled *in situ* inside microfluidic devices and be used as cell culture substrates for "lab-on-chip" technologies. While these self-assembling membranes were designed for bone regeneration, they can also be used in a variety of applications in regenerative medicine, such as skin, cardiac tissue, or cornea, as they can be easily modified to specifically target those tissues.

Conflicts of interest

There are no conflicts to declare.

Acknowledgements

This work was supported by national funds through the Portuguese Foundation for Science and Technology (FCT) under the scope of the project PTDC/CTM-BIO/0814/2012 and by the European Regional Development Fund (ERDF) through the Operational Competitiveness Programme "COMPETE" (FCOMP-01-0124-FEDER-028491). J. Borges and R. P. Pirraco gratefully acknowledge funding support from FCT for post-doctoral (SFRH/BPD/103604/2014) and investigator (IF/00347/2015) grants, respectively. Y. Shi acknowledges China Scholarship Council for her PhD scholarship (no. 201307060020). H. S. Azevedo also acknowledges financial support from the EU-funded project "SuprHApolymers" (PCIG14-GA-2013-631871) and A. Mata acknowledges the

European Research Council Starting Grant "STROFUNSCAFF" and the Marie Curie Career Integration Grant "BIOMORPH".

References

1 K. Piradashvili, E. M. Alexandrino, F. R. Wurm and K. Landfester, *Chem. Rev.*, 2016, **116**, 2141–2169.
2 Y. Zheng, Z. Yu, R. M. Parker, Y. Wu, C. Abell and O. a. Scherman, *Nat. Commun.*, 2014, **5**, 5772.
3 X. Huang, M. Li, D. C. Green, D. S. Williams, A. J. Patil and S. Mann, *Nat. Commun.*, 2013, **4**, 2239.
4 Y. Wang, L. Hosta-Rigau, H. Lomas and F. Caruso, *Phys. Chem. Chem. Phys.*, 2011, **13**, 4782–4801.
5 K. Ohkawa, T. Kitagawa and H. Yamamoto, *Macromol. Mater. Eng.*, 2004, **289**, 33–40.
6 K. Ohkawa, Y. Takahashi, M. Yamada and H. Yamamoto, *Macromol. Mater. Eng.*, 2001, **286**, 168–175.
7 A. L. Becker, A. P. R. Johnston and F. Caruso, *Small*, 2010, **6**, 1836–1852.
8 R. R. Costa, M. Alatorre-meda and J. F. Mano, *Biotechnol. Adv.*, 2015, **33**, 1310–1326.
9 A. Szarpak, D. Cui, F. Dubreuil, B. G. De Geest, L. J. De Cock, C. Picart and R. Auzély-Velty, *Biomacromolecules*, 2010, **11**, 713–720.
10 T. Fujii, D. Ogiwara, K. Ohkawa and H. Yamamoto, *Macromol. Biosci.*, 2005, **5**, 394–400.
11 T. Crouzier, K. Ren, C. Nicolas, C. Roy and C. Picart, *Small*, 2009, **5**, 598–608.
12 L. Gasperini, J. F. Mano and R. L. Reis, *J. R. Soc., Interface*, 2014, **11**, 20140817.
13 G. Decher, *Science*, 1997, **277**, 1232–1237.
14 S. G. Caridade, C. Monge, J. Almodóvar, R. Guillot, J. Lavaud, V. Josserand, J. L. Coll, J. F. Mano and C. Picart, *Acta Biomater.*, 2015, **15**, 139–149.
15 R. M. Capito, H. S. Azevedo, Y. S. Velichko, A. Mata and S. I. Stupp, *Science*, 2008, **319**, 1812–1816.
16 L. W. Chow, R. Bitton, M. J. Webber, D. Carvajal, K. R. Shull, A. K. Sharma and S. I. Stupp, *Biomaterials*, 2011, **32**, 1574–1582.
17 D. S. Ferreira, A. P. Marques, R. L. Reis and H. S. Azevedo, *Biomater. Sci.*, 2013, **1**, 952.
18 D. S. Ferreira, Y.-A. Lin, H. Cui, J. a. Hubbell, R. L. Reis and H. S. Azevedo, *Adv. Healthcare Mater.*, 2015, **4**, 602–612.
19 D. I. Rozkiewicz, B. D. Myers and S. I. Stupp, *Angew. Chem., Int. Ed.*, 2011, **50**, 6324–6327.
20 V. Castelletto, A. Kaur, I. W. Hamley, R. H. Barnes, K.-A. Karatzas, D. Hermida-Merino, S. Swioklo, C. J. Connon, J. Stasiak, M. Reza and J. Ruokolainen, *RSC Adv.*, 2017, **7**, 8366–8375.
21 J. Borges, M. P. Sousa, G. Cinar, S. G. Caridade, M. O. Guler and J. F. Mano, *Adv. Funct. Mater.*, 2017, 1605122.
22 K. E. Inostroza-Brito, E. Collin, O. Siton-Mendelson, K. H. Smith, A. Monge-Marcet, D. S. Ferreira, R. Pérez Rodríguez, M. Alonso, J. C. Rodríguez-Cabello, R. L. Reis, F. Sagués, L. Botto, R. Bitton, H. S. Azevedo and A. Mata, *Nat. Chem.*, 2015, **7**, 1–8.
23 A. C. Mendes, K. H. Smith, E. Tejeda-Montes, E. Engel, R. L. Reis, H. S. Azevedo and A. Mata, *Adv. Funct. Mater.*, 2013, **23**, 430–438.
24 H. Dong, S. E. Paramonov, L. Aulisa, E. L. Bakota and J. D. Hartgerink, *J. Am. Chem. Soc.*, 2007, **129**, 12468–12472.
25 L. Aulisa, H. Dong and J. D. Hartgerink, *Biomacromolecules*, 2009, **10**, 2694–2698.
26 M. K. Kang, J. S. Colombo, R. N. D'Souza and J. D. Hartgerink, *Biomacromolecules*, 2014, **15**, 2004–2011.
27 E. L. Bakota, O. Sensoy, B. Ozgur, M. Sayar and J. D. Hartgerink, *Biomacromolecules*, 2013, **14**, 1370–1378.
28 V. A. Kumar, N. L. Taylor, S. Shi, B. K. Wang, A. A. Jalan, M. K. Kang, N. C. Wickremasinghe and J. D. Hartgerink, *ACS Nano*, 2015, **9**, 860–868.
29 P. van Rijn, M. Tutus, C. Kathrein, L. Zhu, M. Wessling, U. Schwaneberg and A. Böker, *Chem. Soc. Rev.*, 2013, **42**, 6578.
30 A. George and A. Veis, *Chem. Rev.*, 2009, **108**, 4670–4693.
31 E. Ruoslahti and M. D. Pierschbacher, *Cell*, 1986, **44**, 517–518.
32 I. Bab, D. Gazit, M. Chorev, A. Muhlrad, A. Shteyer, Z. Greenberg, M. Namdar and A. Kahn, *EMBO J.*, 1992, **11**, 1867–1873.
33 C. J. Newcomb, R. Bitton, Y. S. Velichko, M. L. Snead and S. I. Stupp, *Small*, 2012, **8**, 2195–2202.
34 F. R. Maia, M. Barbosa, D. B. Gomes, N. Vale, P. Gomes, P. L. Granja and C. C. Barrias, *J. Controlled Release*, 2014, **189**, 158–168.
35 I. Bab, H. Gavish, M. Namdar-Attar, a. Muhlrad, Z. Greenberg, Y. Chen, N. Mansur, a. Shteyer and M. Chorev, *J. Pept. Res.*, 1999, **54**, 408–414.
36 S. M. S. Miguel, M. Namdar-Attar, T. Noh, B. Frenkel and I. Bab, *J. Biol. Chem.*, 2005, **280**, 37495–37502.
37 N. Gabarin, H. Gavish, A. Muhlrad, Y. Chen, M. Namdar-Attar, R. A. Nissenson, M. Chorev and I. Bab, *J. Cell. Biochem.*, 2001, **81**, 594–603.
38 Y. Gabet, R. Müller, E. Regev, J. Sela, A. Shteyer, K. Salisbury, M. Chorev and I. Bab, *Bone*, 2004, **35**, 65–73.
39 G. M. Policastro and M. L. Becker, *Wiley Interdiscip. Rev.: Nanomed. Nanobiotechnol.*, 2016, **8**, 449–464.
40 A. Horii, X. Wang, F. Gelain and S. Zhang, *PLoS One*, 2007, **2**, 1–9.
41 N. M. Moore, N. J. Lin, N. D. Gallant and M. L. Becker, *Biomaterials*, 2010, **31**, 1604–1611.
42 H. Zhu, B. Cao, Z. Zhen, A. A. Laxmi, D. Li, S. Liu and C. Mao, *Biomaterials*, 2011, **32**, 4744–4752.
43 S. Panseri, L. Russo, M. Montesi, F. Taraballi, C. Cunha, M. Marcacci and L. Cipolla, *MedChemComm*, 2014, **5**, 899–903.
44 H. Chang and M. L. Knothe Tate, *Stem Cells Transl. Med.*, 2012, **1**, 480–491.
45 J. Eyckmans, G. L. Lin and C. S. Chen, *Biol. Open*, 2012, **1**, 1058–1068.

46 A. Oyane, H.-M. Kim, T. Furuya, T. Kokubo, T. Miyazaki and T. Nakamura, *J. Biomed. Mater. Res., Part A*, 2003, **65**, 188–195.
47 T. Kokubo and H. Takadama, *Biomaterials*, 2006, **27**, 2907–2915.
48 T. Kokubo, *Mater. Sci. Eng., C*, 2005, **25**, 97–104.
49 A. C. Mendes, E. T. Baran, R. L. Reis and H. S. Azevedo, *Wiley Interdiscip. Rev.: Nanomed. Nanobiotechnol.*, 2013, **5**, 582–612.
50 N. Stephanopoulos, J. H. Ortony and S. I. Stupp, *Acta Mater.*, 2013, **61**, 912–930.
51 D. W. Löwik and J. C. van Hest, *Chem. Soc. Rev.*, 2004, **33**, 234–245.
52 X. Wang, A. Horii and S. Zhang, *Soft Matter*, 2008, **4**, 2388.
53 Molinspiration Cheminformatics, http://www.molinspiration.com/.
54 S. Weiner and L. Addadi, *J. Mater. Chem.*, 1997, **7**, 689–702.
55 G. K. Toworfe, R. J. Composto, I. M. Shapiro and P. Ducheyne, *Biomaterials*, 2006, **27**, 631–642.
56 W. Habraken, P. Habibovic, M. Epple and M. Bohner, *Mater. Today*, 2016, **19**, 69–87.
57 A. J. Engler, S. Sen, H. L. Sweeney and D. E. Discher, *Cell*, 2006, **126**, 677–689.
58 S. Walcott and S. X. Sun, *Proc. Natl. Acad. Sci. U. S. A.*, 2010, **107**, 7757–7762.
59 Z. X. Chen, M. Chang, Y. L. Peng, L. Zhao, Y. R. Zhan, L. J. Wang and R. Wang, *Regul. Pept.*, 2007, **142**, 16–23.
60 E. A. Cavalcanti-Adam, A. Micoulet, J. Blümmel, J. Auernheimer, H. Kessler and J. P. Spatz, *Eur. J. Cell Biol.*, 2006, **85**, 219–224.
61 G. A. Silva, C. Czeisler, K. L. Niece, E. Beniash, D. A. Harrington, J. A. Kessler and S. I. Stupp, *Science*, 2004, **303**, 1352–1355.
62 E. Tejeda-montes, A. Klymov, M. R. Nejadnik, M. Alonso, J. C. Rodriguez-cabello, X. F. Walboomers and A. Mata, *Biomaterials*, 2014, **35**, 8339–8347.
63 J. Liu and D. G. Kerns, *Open Dent. J.*, 2014, **8**, 56–65.

